

THE WEAK LENSING SIGNAL AND THE CLUSTERING OF BOSS GALAXIES I: MEASUREMENTS

HIRONAO MIYATAKE^{1,2}, SURHUD MORE², RACHEL MANDELBAUM³, MASAHIRO TAKADA², DAVID N. SPERGEL¹, JEAN-PAUL KNEIB^{4,5},
DONALD P. SCHNEIDER^{6,7}, J. BRINKMANN⁸, JOEL R. BROWNSTEIN⁹

¹ Department of Astrophysical Sciences, Princeton University, Peyton Hall, Princeton NJ 08544, USA

² Kavli Institute for the Physics and Mathematics of the Universe (WPI), The University of Tokyo, Chiba 277-8582, Japan

³ McWilliams Center for Cosmology, Department of Physics, Carnegie Mellon University, Pittsburgh, PA 15213, USA

⁴ Aix Marseille Université, CNRS, LAM (Laboratoire d'Astrophysique de Marseille) UMR 7326, 13388, Marseille, France

⁵ Laboratoire d'astrophysique, École Polytechnique Fédérale de Lausanne (EPFL), Observatoire de Sauverny, 1290 Versoix, Switzerland

⁶ Department of Astronomy and Astrophysics, The Pennsylvania State University, University Park, PA 16802, USA

⁷ Institute for Gravitation and the Cosmos, The Pennsylvania State University, University Park, PA 16802, USA

⁸ Apache Point Observatory, PO Box 59 Sunspot, NM 88349, USA

⁹ Department of Physics and Astronomy, University of Utah, 115 S 1400 E, Salt Lake City, UT 84112, USA

Accepted for publication in the Astrophysical Journal

ABSTRACT

A joint analysis of the clustering of galaxies and their weak gravitational lensing signal is well-suited to simultaneously constrain the galaxy-halo connection as well as the cosmological parameters by breaking the degeneracy between galaxy bias and the amplitude of clustering signal. In a series of two papers, we perform such an analysis at the highest redshift ($z \sim 0.53$) in the literature using CMASS galaxies in the Sloan Digital Sky Survey-III Baryon Oscillation Spectroscopic Survey Eleventh Data Release (SDSS-III/BOSS DR11) catalog spanning 8300 deg^2 . In this paper, we present details of the clustering and weak lensing measurements of these galaxies. We define a subsample of 400,916 CMASS galaxies based on their redshifts and stellar mass estimates so that the galaxies constitute an approximately volume-limited and similar population over the redshift range $0.47 \leq z \leq 0.59$. We obtain a signal-to-noise ratio $S/N \approx 56$ for the galaxy clustering measurement. We also explore the redshift and stellar mass dependence of the clustering signal. For the weak lensing measurement, we use existing deeper imaging data from the CFHTLS with publicly available shape and photometric redshift catalogs from CFHTLenS, but only in a 105 deg^2 area which overlaps with BOSS. This restricts the lensing measurement to only 5,084 CMASS galaxies. After careful systematic tests, we find a highly significant detection of the CMASS weak lensing signal, with total $S/N \approx 26$. These measurements form the basis of the halo occupation distribution and cosmology analysis presented in More et al. (Paper II).

Subject headings: gravitational lensing — galaxies

1. INTRODUCTION

In the current concordance cosmological model (Λ CDM), dark matter and dark energy constitute a large fraction ($\sim 95.5\%$) of the energy density of the Universe; this conclusion is supported by a growing body of diverse observational astrophysical evidence (see e.g., Hinshaw et al. 2013; Planck Collaboration et al. 2013; Sullivan et al. 2011; Suzuki et al. 2012; Rest et al. 2013; Blake et al. 2011; Beutler et al. 2011; Anderson et al. 2012; Aubourg et al. 2014; Reid et al. 2012). Yet, we have little theoretical understanding of the fundamental physics that governs the physics of dark matter or dark energy. For this reason a large number of wide-area galaxy surveys are ongoing or planned for the near future aimed at characterizing the dark matter distribution and understanding the nature of dark energy. These include both the imaging and spectroscopic surveys: the Kilo-Degrees Survey (KIDS)¹, the Subaru Hyper Suprime-Cam (HSC) Survey² (see also Miyazaki et al. 2012), the Dark Energy Survey (DES)³, Extended Baryon Oscillation Spectroscopic Survey (eBOSS)⁴, Subaru Prime Focus Spectrograph (PFS) Survey⁵ (see also Takada et al. 2014), Dark Energy Spectroscopic Instrument

(DESI)⁶, and ultimately the Large Synoptic Survey Telescope (LSST)⁷ (see also LSST Science Collaboration et al. 2009), the Euclid project⁸, and the Wide-Field Infrared Survey Telescope (WFIRST) project⁹ (see also Spergel et al. 2013).

The measurement of galaxy clustering statistics is one of the most powerful probes in observational cosmology (Tegmark et al. 2004; Cole et al. 2005; Percival et al. 2010; Zehavi et al. 2011; Saito et al. 2011; Reid et al. 2012, 2014; Samushia et al. 2014). However, our lack of a detailed understanding of the relationship between the distribution of galaxies and that of dark matter limits the full use of the measured amplitude of the clustering signal for constraining cosmological parameters. Seljak et al. (2005) first proposed and demonstrated that it is possible to break this degeneracy between the unknown bias between galaxies and matter and the cosmological parameters by utilizing the theoretical dependence of galaxy bias on halo mass (Mo & White 1996; Sheth & Tormen 1999). By probing the halo masses of galaxies via the weak gravitational lensing around galaxies, commonly referred to as galaxy-galaxy lensing, on small scales (see also Yoo et al. 2006; Cacciato et al. 2009; Li et al. 2009; Tinker et al. 2012; Leauthaud et al. 2012; More et al. 2013; Cac-

¹ <http://www.astro-wise.org/projects/KIDS/>

² <http://www.naoj.org/Projects/HSC/index.html>

³ <http://www.darkenergysurvey.org>

⁴ <https://www.sdss3.org/future/eboss.php>

⁵ <http://sumire.ipmu.jp/pfs/intro.html>

⁶ <http://desi.lbl.gov>

⁷ <http://www.lsst.org/lsst/>

⁸ <http://sci.esa.int/science-e/www/area/index.cfm?fareaid=102>

⁹ <http://wfirst.gsfc.nasa.gov>

ciato et al. 2013b; Gillis et al. 2013; Cacciato et al. 2013a; Simpson et al. 2013) (see also Fischer et al. 2000; Mandelbaum et al. 2006; van Uitert et al. 2011; Velander et al. 2013, for the galaxy-galaxy lensing measurements). An alternative method, which uses the ratio of the clustering and lensing signals, has also been proposed in order to avoid the complex astrophysics that complicates the interpretation of these observables on scales smaller than the typical halo radii (Baldauf et al. 2010). As a proof of this concept, Mandelbaum et al. (2013, hereafter RM13) used the state-of-the-art measurement of galaxy-galaxy lensing signal and galaxy clustering up to large scales ($\sim 70 h^{-1}\text{Mpc}$) by combining the spectroscopic and multi-color imaging galaxy catalogs from the Sloan Digital Sky Survey I/II (SDSS I/II; York et al. 2000; Eisenstein et al. 2001; Strauss et al. 2002). They showed that the joint analysis provides a significant improvement in the cosmological parameters Ω_m and σ_8 when combined with results from the WMAP7 experiment (Komatsu et al. 2011).

The purpose of this paper and our companion paper (More et al. 2014, hereafter Paper II) is to extend the joint clustering and lensing analysis to galaxies at $z \sim 0.5$ and then place constraints on cosmological parameters Ω_m and $\sigma_8(z)$ at the redshift. This study is at the highest redshift among such kind of measurements in the literature. To do this, we use independent data sets to measure the clustering and weak lensing signals: the Baryon Oscillation Spectroscopic Survey (BOSS; Schlegel et al. 2009; Dawson et al. 2013), which is in a part of the SDSS-III (SDSS-III; Eisenstein et al. 2011), and the publicly-available Canada-France-Hawaii Telescope Lensing Survey (CFHTLenS; Heymans et al. 2012) catalog.

The BOSS survey is measuring spectroscopic redshifts of 1.5 millions galaxies, approximately volume limited to $z \simeq 0.6$. The BOSS galaxies, the so-called CMASS (“constant mass”) galaxies, are selected from the multi-color SDSS imaging data based on the requirements that the number density of the CMASS galaxies, with successful redshifts measurements, is high enough to probe large-scale structure at an intermediate redshift around $z \sim 0.5$. The CFHTLenS catalog contains galaxies with a median redshift of $z \sim 0.7$, where every galaxy has its shape and photometric redshift (photo- z) information estimated using the carefully designed point-spread-function-matched photometry of different pass-band data (Hildebrandt et al. 2012). Thus the CFHTLenS catalog is best suited for our purpose because it is much deeper and therefore contains a higher number density of source galaxies than in the SDSS (Abazajian et al. 2009). In addition the photo- z information allows a selection of source galaxies which can be used to measure the weak gravitational lensing signal of the CMASS galaxies, even though the overlapping region of the two surveys is only ~ 105 square degrees, about one hundredth of the SDSS area.

In our analysis, we define subsamples of the parent CMASS catalog based on their stellar mass estimates so that the galaxies constitute a physically similar population over the redshift range $0.47 \leq z \leq 0.59$. We will use the different subsamples, defined with different stellar mass thresholds and in different redshift bins, to test how the clustering and lensing signals of galaxies vary as a function of redshift and stellar mass. Then we will use different stellar mass threshold subsamples to test possible effects of the incompleteness or selection inhomogeneities at the low stellar mass end on our cosmological constraints. This paper, the first in a series of two, will present the details of the subsamples and the clustering and lensing measurements. In Paper II we will present the constraints on

the halo occupation distribution of galaxies and cosmological parameters derived from the measurements.

The structure of this paper is as follows. In Section 2, we describe the BOSS data used in this paper, the definition of our subsamples constructed from the parent CMASS catalog, and details of the clustering signal measurements. In Section 3, we describe the CFHTLenS data used in our lensing measurement, details of our weak lensing analysis methodology, and the systematic tests of the CFHTLenS catalog using random catalogs. Section 4 is devoted to discussion and conclusions. Unless stated otherwise, we will adopt a flat Λ CDM cosmology with $\Omega_m = 0.27$, $\Omega_\Lambda = 0.73$, and the Hubble parameter $h = H_0/(100 \text{ km s}^{-1} \text{ Mpc}^{-1}) = 0.703$.

2. SDSS-III BOSS DATA AND CLUSTERING MEASUREMENTS

2.1. SDSS-III BOSS galaxies

For the clustering measurements, we use the sample of galaxies compiled in Data Release 11 (DR11) of the SDSS-III project. The SDSS-III is a spectroscopic investigation of galaxies and quasars selected from the imaging data obtained by the SDSS (York et al. 2000) I/II covering about $11,000 \text{ deg}^2$ (Abazajian et al. 2009) using the dedicated 2.5-m SDSS Telescope (Gunn et al. 2006). The imaging employed a drift-scan mosaic CCD camera (Gunn et al. 1998) with five photometric bands (u, g, r, i and z) (Fukugita et al. 1996; Smith et al. 2002; Doi et al. 2010). The SDSS-III (Eisenstein et al. 2011) BOSS project (Ahn et al. 2012; Dawson et al. 2013) obtained additional imaging data of about $3,000 \text{ deg}^2$ (Aihara et al. 2011). The imaging data was processed by a series of pipelines (Lupton et al. 2001; Pier et al. 2003; Padmanabhan et al. 2008) and corrected for Galactic extinction (Schlegel et al. 1998) to obtain a reliable photometric catalog. This catalog was used as an input to select targets for spectroscopy (Dawson et al. 2013) for conducting the BOSS survey (Ahn et al. 2012) with the SDSS spectrographs (Smee et al. 2013). Targets are assigned to tiles of diameter 3° using an adaptive tiling algorithm designed to maximize the number of targets that can be successfully observed (Blanton et al. 2003). The resulting data were processed by an automated pipeline which performs spectral classification, redshift determination, and various parameter measurements, e.g., the stellar mass measurements from a number of different stellar population synthesis codes which utilize the photometry and redshifts of the individual galaxies (Bolton et al. 2012). In addition to the galaxies targeted by the BOSS project, we also use galaxies which pass the target selection but have already been observed as part of the SDSS-I/II project (legacy galaxies). These legacy galaxies are subsampled in each sector so that they obey the same completeness as that of the CMASS sample (Anderson et al. 2014).

To perform measurements of the clustering and lensing signals, we create various subsamples of the parent large scale structure catalog provided with DR11. To define the subsamples we use for the analysis, we make use of the stellar masses processed through the Portsmouth stellar population synthesis code (Maraston et al. 2013) with the assumptions of a passively evolving stellar population synthesis model and a Kroupa (2001) initial mass function. The upper panel of Figure 1 shows the distribution of a random subsample of all galaxies in the large scale structure catalog in the stellar mass-redshift plane. The number density of this sample varies as a function of redshift and peaks at $z \sim 0.5$, as shown

in the bottom panel. The fiducial subsample we use in this paper, denoted as subsample A, consists of all galaxies between $z \in [0.47, 0.59]$ and with $\log M_*/h_{70}^{-2} M_\odot \in [11.1, 12.0]$. This selection results in a sample with an approximately uniform number density with redshift compared to the parent sample, as shown by the black dashed line in the lower panel of Figure 1. The number density of this fiducial subsample is $\sim 3 \times 10^{-4} h^3 \text{ Mpc}^{-3}$. The total number of galaxies in this subsample is 378 807 (400 916)¹⁰ and constitutes about half of the parent sample used for the measurements of the baryon acoustic oscillations. In order to test the effects of incompleteness at the low stellar mass end in our fiducial subsample, we additionally consider two different subsamples of galaxies which lie in the same redshift range but where the stellar mass selection is $\log M_*/h_{70}^{-2} M_\odot \in [11.30, 12.0]$ and $\log M_*/h_{70}^{-2} M_\odot \in [11.40, 12.0]$, respectively. These subsamples will be denoted as *B* and *C*, respectively. The numbers of galaxies in these subsamples are 196 578 and 116 682 (these numbers include fiber collided and redshift failure galaxies), while the number densities of the galaxies are 1.5×10^{-4} and $0.8 \times 10^{-4} h^3 \text{ Mpc}^{-3}$, respectively. The number density of galaxies is approximately constant in the redshift range we use. In addition to these subsamples, we will also consider subsamples in different redshift bins to test the redshift and stellar mass dependence of the clustering signals.

We must account for a number of subtle selection effects in order to obtain a precise measurement of clustering (Ross et al. 2012). The spectroscopic target sample is obtained from the SDSS imaging observations after the application of a variety of colour and photometric selection cuts (Dawson et al. 2013). However, due to the limited number of fibers available, not all galaxies from this target sample can be allocated a fiber while performing spectroscopic observations to determine their redshifts. This could also happen if two targets are within $62''$ of each other and hence they cannot be simultaneously observed due to the finite size of fibers. If such fiber-collided galaxies lie in a region of the sky which is visited multiple times (due to overlaps in the target tiling) then they may have redshift measurements. There are also instances where a galaxy is assigned to a fiber, but its redshift could not be obtained. Finally, there are also instances where it is difficult to perform star-galaxy separation, especially in fields with a high number density of stars. These effects have been quantified in the parent DR11 catalog of CMASS galaxies by assigning a weight to each galaxy such that

$$w_1 = w_* (w_{\text{noz}} + w_{\text{cp}} - 1), \quad (1)$$

where w_{noz} is the weight assigned to a galaxy if it is the nearest neighbour (in the plane of the sky) of a redshift failure galaxy, w_{cp} is similarly assigned to account for the nearest neighbours of fiber collided galaxies¹¹, and w_* accounts for the systematic relationship between density of stars and density of BOSS target galaxies (for details, see Anderson et al. 2014). The BOSS parent catalog contains an additional weight, w_{FKP} , for each galaxy which depends upon the number density of galax-

ies in the sample at its redshift (Feldman et al. 1994). This weight is important for the parent galaxy catalog which has a much larger variation in the number density of galaxies than the variation in $\bar{n}(z)$ for the subsamples of galaxies we use. Therefore, in our analysis, we do not include this weight.

The weights w_{noz} and w_{cp} can only be used if the entire sample of galaxies within a given redshift range is used to measure the clustering signal. In particular, for the subsamples of galaxies selected by stellar mass (or luminosity), it is unclear whether the fiber-collided or redshift-failure galaxy will be part of our subsample if it is assigned the same redshift as its nearest neighbour, as it may or may not satisfy the stellar mass cut we have imposed. If we were to use the weights w_{noz} and w_{cp} as provided, then we would spuriously include the weights of some galaxies which should not be in the subsample. We will also miss some fiber-collided or redshift-failure galaxies which should have been part of our subsample because their nearest neighbours failed to make it to our subsample due to stellar mass cuts. In addition there is a possibility that the small scale clustering will be affected by using the weights, as all pairs of galaxies involving a fiber-collided or redshift-failure galaxy are assigned line-of-sight separations equal to zero.

Given these issues, we refrain from using the weights w_{noz} and w_{cp} in our analysis. Instead, we have obtained the stellar masses using the measured photometry of the fiber-collided and the redshift-failure galaxies with the redshift of its nearest neighbour. Each of these galaxies are assigned the same w_* as their nearest neighbours. We have verified that the stellar mass-redshift distribution of such galaxies is similar to that of the sample of galaxies which have well measured redshifts (catastrophic failures in the nearest neighbour redshift assumption will result in both a incorrect redshift and stellar mass). We then decide whether to include these galaxies in our subsample based on whether these galaxies pass the stellar mass cuts we impose. Given our treatment of fiber collided galaxies, the only weight we have to use in our analysis is

$$w_1 = w_*. \quad (2)$$

2.2. CMASS galaxy clustering measurements

The clustering of galaxies can be quantified using the two-point correlation function. The two-point correlation function, $\xi(r)$, depends only upon the true three-dimensional distance between galaxies, r , if the Universe is isotropic. However, the assumption of isotropy is broken due to the modulation of the distances of galaxies along the line-of-sight (π) caused by the peculiar motions of galaxies. In contrast, the distances along the plane of the sky (r_p) do not suffer from this modulation. The resultant correlation function displays a characteristic anisotropic pattern which elongates (flattens) the iso-correlation contours in the (r_p, π) plane on small (large) projected scales. The impact of such effects can be minimized by focusing on the projected two-point correlation function obtained by integrating the correlation function $\xi(r_p, \pi)$ along the line-of-sight,

$$w_p(r_p) = 2 \int_0^{\pi_{\text{max}}} \xi(r_p, \pi) d\pi. \quad (3)$$

Unless stated otherwise, we will use $\pi_{\text{max}} = 100 h^{-1} \text{ Mpc}$, and employ the same finite line-of-sight integration limit while analytically modelling the observations in Paper II. When calculating the integral, we adopted the binning of $\Delta\pi = 1 h^{-1} \text{ Mpc}$.

¹⁰ The number in parentheses includes galaxies with redshift failures and those that could not be allocated fibers to measure their redshifts (fiber collided galaxies) as described in the next paragraph.

¹¹ Nearest neighbour corrections have been shown to accurately correct for fiber collisions above the fiber collision scale ($\sim 0.4 h^{-1} \text{ Mpc}$) by Guo et al. (2012). Both w_{noz} and w_{cp} are equal to unity by default for all galaxies. Their values are incremented for the nearest neighbours of every redshift failure or fiber collided galaxy.

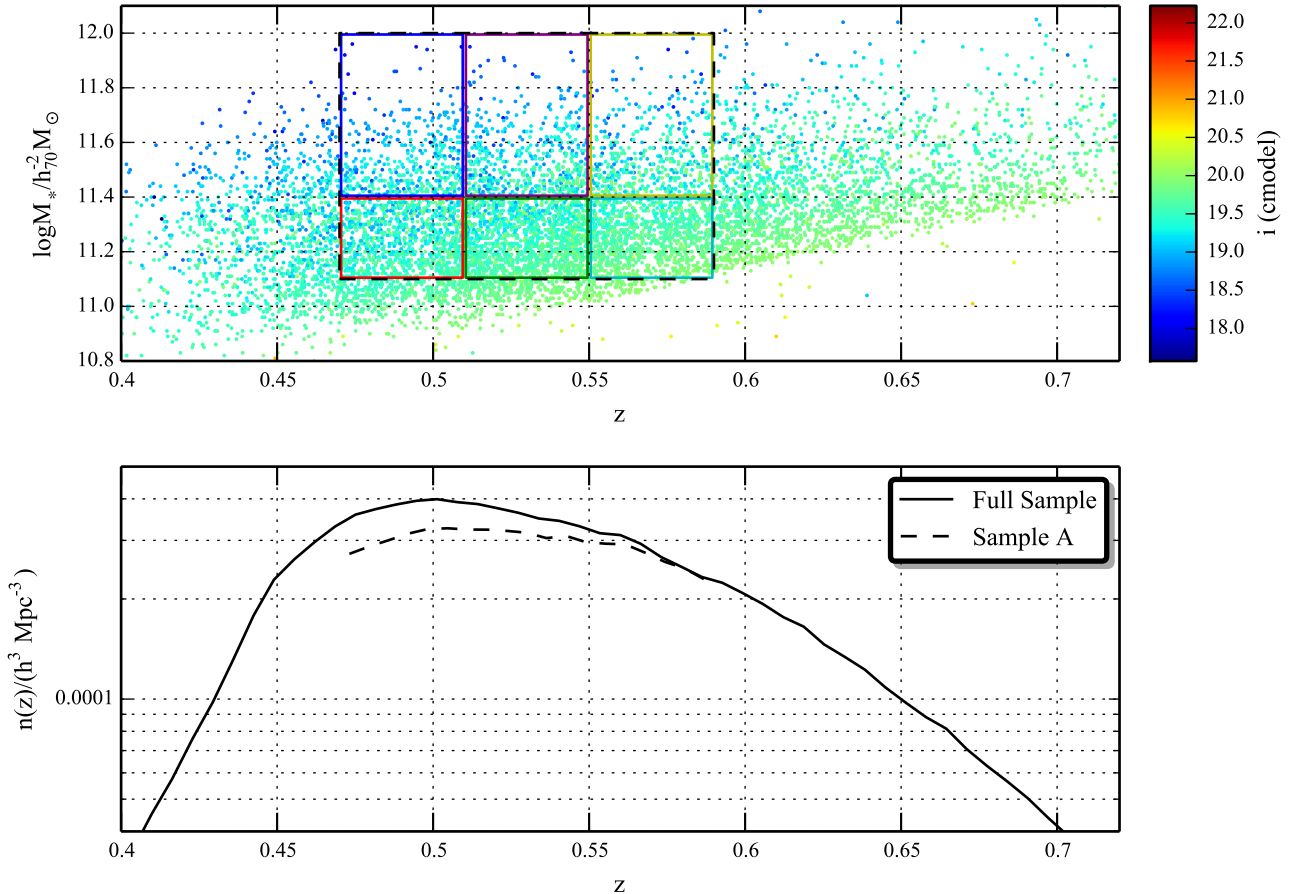


Figure 1. *Upper panel:* The CMASS galaxy sample in the redshift–stellar mass plane. The fiducial subsample (here after subsample A) used in this study corresponds to the redshift range $z \in [0.47, 0.59]$ and stellar mass range $\log M_* \in [11.1, 12.0]$, which is shown as the black dashed box. To investigate the redshift and stellar mass dependence of the clustering we further subdivide this subsample into six bins indicated by different colour boxes in this figure. In addition, we will investigate the robustness of the cosmological constraints with different subsamples that span the same redshift range as our fiducial subsample but progressively restricting the samples to more massive galaxies, $\log M_* \in [11.3, 12.0]$ and $\log M_* \in [11.4, 12.0]$. Hereafter we call these subsamples of higher stellar mass thresholds, subsample B and C, respectively. To avoid crowding we show only 10,000 galaxies from the total CMASS galaxies in this figure. Colors of each point denote the i -band cmodel magnitudes in the SDSS imaging catalog. *Lower panel:* The redshift dependence of the comoving number density. The dashed curve shows our fiducial subsample, which is almost constant in the redshift range centered at $z \approx 0.53$. For comparison, the solid curve shows the full CMASS sample.

We use the estimator proposed by Landy & Szalay (1993),

$$\xi(r_p, \pi) = \frac{DD - 2DR + RR}{RR} \quad (4)$$

to obtain the two-point correlation function $\xi(r_p, \pi)$. Here, DD , RR and DR represent the number of appropriately weighted pairs of galaxies with a given separation (r_p, π) , where both galaxies lie either in the galaxy catalog or the random catalog or one in each of the catalogs, respectively.

We use random catalogues with the same angular and redshift selection as our galaxy subsample. These random catalogs consist of about 50 times more points than the number of galaxies in each of our subsamples. We assign each random point a weight of $N_{\text{gal}}/N_{\text{ran}}$ to account for this difference. In practice, we use the random catalogs provided with SDSS DR11 (Anderson et al. 2014). We subsample these random catalogs in order to tailor them to the CMASS subsamples we use. For this purpose, we first divide the entire CMASS catalog into narrow redshift bins ($\Delta z = 0.05$). For each bin we calculate the fraction of galaxies in our subsample after the stellar mass and redshift cuts are applied to the total sample, and interpolate this fraction as a function of redshift. This

fraction is used at each redshift as the probability to accept points from the random catalog. This procedure also automatically accounts for the redshift cuts as the fraction outside the redshift range we have chosen is identically equal to zero.

In Figure 2, we explore the stellar mass and redshift dependence of the clustering signal. For this purpose, we use the galaxy subsamples enclosed in the six color boxes in Figure 1. Each panel shows the dependence of the clustering signal on stellar mass selection at fixed redshift¹². This figure demonstrates that the clustering signal varies with stellar mass at fixed redshift. Given that the stellar mass threshold of the full sample of CMASS galaxies varies with redshift, the stellar mass dependence of the clustering signal implies the necessity of a proper redshift dependent modelling of the clustering if the entire galaxy sample is used. In Figure 3, we show that the clustering signals of the stellar mass limited subsamples do not vary substantially with redshift. Although

¹² We use a line-of-sight integration length $\pi_{\text{max}} = 60 h^{-1} \text{Mpc}$ for projecting the redshift space correlation function for these tests only given the limited redshift range of the data. Everywhere else in the paper we use $\pi_{\text{max}} = 100 h^{-1} \text{Mpc}$.

not a formal justification, this result supports our assumption of a single effective redshift for modelling our measurements. For our main analysis, we will therefore focus on subsamples A, B and C that are defined by constant stellar mass thresholds in the redshift range $z \in [0.47, 0.59]$.

We show the projected clustering signals for subsamples A, B and C of the CMASS galaxies in Figure 4. The errorbars are obtained using the jackknife technique, where we utilized 192 jackknife regions on the sky covering the entire survey footprint. The cross-correlation matrix of the projected clustering measurement in each of our subsamples (normalized to have a value of unity on the diagonals) are shown in each of the panels of Figure 5. The correlation coefficients are defined as

$$C_{ij} = \frac{\text{Cov}(i, j)}{\sqrt{\text{Cov}(i, i)\text{Cov}(j, j)}}, \quad (5)$$

where the subscripts i, j denotes the radial bin index.

We observe that there is a significant covariance between the errorbars of the measurements on large scales, and we include this covariance while modelling the signal. The total signal-to-noise ratio of the clustering in our fiducial subsample is 55.6, properly accounting for the covariance. It decreases to total signal-to-noise ratios of 48.3 and 39.7 for the subsamples B and C, respectively. The right panel of Figure 4 shows the lensing signal of our CMASS subsample. The details of this measurement are described in the next section.

3. CFHTLENS DATA AND LENSING MEASUREMENT

3.1. CFHTLenS catalog

For the measurements of the galaxy-galaxy lensing signal around the subsamples of CMASS galaxies, we must measure the tangential distortion of background galaxies. For this purpose, we rely on the deeper and better quality imaging data from the Canada France Hawaii Telescope Legacy Survey (CFHTLS). This information allows us to measure the tangential distortion of background galaxies around the different subsamples of CMASS galaxies. In particular we make use of the photometric reduction and image shape determinations in the publicly available CFHTLenS catalog¹³. Unfortunately, the overlap between the CFHTLS and the DR11 BOSS fields is limited to an area of only $\sim 100 \text{ deg}^2$. The number of CMASS galaxies that lie within the CFHTLS footprint is 5,084 for our fiducial subsample A, 2,549 from subsample B and 1,577 for subsample C, compared to ~ 0.4 million CMASS galaxies in the entire BOSS footprint. In Figure 6, we show the different CFHTLS fields. The positions of CMASS galaxies in subsample A within these fields are indicated by black dots.

The quantities needed for shape estimate of each galaxy image, its ellipticity, calibration factors, and weight are provided in the CFHTLenS catalog (Heymans et al. 2012; Erben et al. 2013; Miller et al. 2013). The two ellipticity components in the celestial coordinate system, (e_1, e_2) , were estimated from the i' -band data of each galaxy image using the *lensfit* software, which is based on a Bayesian model-fitting method (Miller et al. 2007) for a model with two components. The ellipticity is defined as $e = (a - b) / (a + b)$, where a and b are the major and minor axes of the ellipse, respectively. Using a shear recovery test based on galaxy image simulations, the CFHTLenS team also provided calibration factors that are

a function of galaxy size and detection signal-to-noise ratio, so that the input shear for simulated galaxy images is recovered to the desired accuracy after application of these factors. The calibration factors consist of the shear multiplicative bias factor m , which is commonly applied to both e_1 and e_2 , and the additive term c_2 , which is applied to e_2 alone. The shear correction is greater for a galaxy with small signal-to-noise ratio and small scale-radius (size). We will describe the details of the shear calibration scheme in Section 3.2. The inverse-variance weight for each galaxy is defined by the variance that is estimated from the intrinsic galaxy ellipticity and the measurement error due to photon noise (for details, see Miller et al. 2013).

Photo- z for each source galaxy were estimated with the *BPZ* code (Benítez 2000; Coe et al. 2006) by using PSF-matched photometry that aims at measuring aperture photometry for the same physical part of each galaxy in different passbands (for details, see Hildebrandt et al. 2012). The BPZ code provides a probability distribution function (PDF) of the photo- z estimate for each galaxy (hereafter $P(z)$). We make use of the full information of $P(z)$ when computing lensing signal.

To make a reliable lensing measurement, we use the following catalog of source galaxies. First, we discard galaxies that have the flag `MASK > 1` indicating masked objects. We use the galaxies that have the ellipticity weight `weight > 0`, and the ellipticity fitting flag `fitclass = 0`, which indicates that the shape is reliably estimated. We do not apply any cut to magnitude or signal-to-noise ratio, i.e., we use all the faint galaxies as long as the above conditions are satisfied. Although the faint galaxies are highly downweighted and largely corrected for the calibration factors, they contribute to the lensing signal and slightly increase the signal-to-noise ratio.

3.2. Galaxy-galaxy lensing measurements

Galaxy-galaxy weak lensing measures a coherent distortion of source galaxy shapes due to all matter around lens galaxies, including dark matter (see Mandelbaum et al. 2013, and references therein). The lensing signal is only statistically measurable and can be estimated by stacking tangential component of source galaxy ellipticities with respect to the position of lens galaxy, for all the pairs of lens and source galaxies in each circular annulus. The lensing distortion profile probed in this way is expressed in terms of the projected surface mass density profile of the average mass distribution around the lens galaxies:

$$\gamma_t(R) = \frac{\Delta\Sigma(R)}{\Sigma_{\text{cr}}} = \frac{\bar{\Sigma}(<R) - \Sigma(R)}{\Sigma_{\text{cr}}}, \quad (6)$$

where R is the projected separation between the source and lens galaxies at the redshift of each lens galaxy, $\Sigma(R)$ is the projected mass density profile at radius R , $\bar{\Sigma}(<R)$ is the average mass density within a circle of radius R , and Σ_{cr} is the critical surface mass density. A spectroscopic redshift for each CMASS galaxy, z_1 , enables an estimation of the projected radius from the observed angle separation $\Delta\theta$ via $R = d_A(z_1)\Delta\theta$, where $d_A(z_1)$ is the comoving angular diameter distance to the lens galaxy. The critical density Σ_{cr} for lens and source galaxies at redshifts z_1 and z_s , respectively, is defined as

$$\Sigma_{\text{cr}}^{-1}(z_1, z_s) = \frac{4\pi G}{c^2} \frac{d_A(z_1)d_A(z_s)(1+z_1)^2}{d_A(z_s)}. \quad (7)$$

Here $d_A(z_s)$, $d_A(z_1)$ and $d_A(z_1, z_s)$ are the angular diameter distances for the source-lens system. The factor of $(1+z_1)^2$ arises

¹³ <http://www.cfhtlens.org/astronomers/data-store>

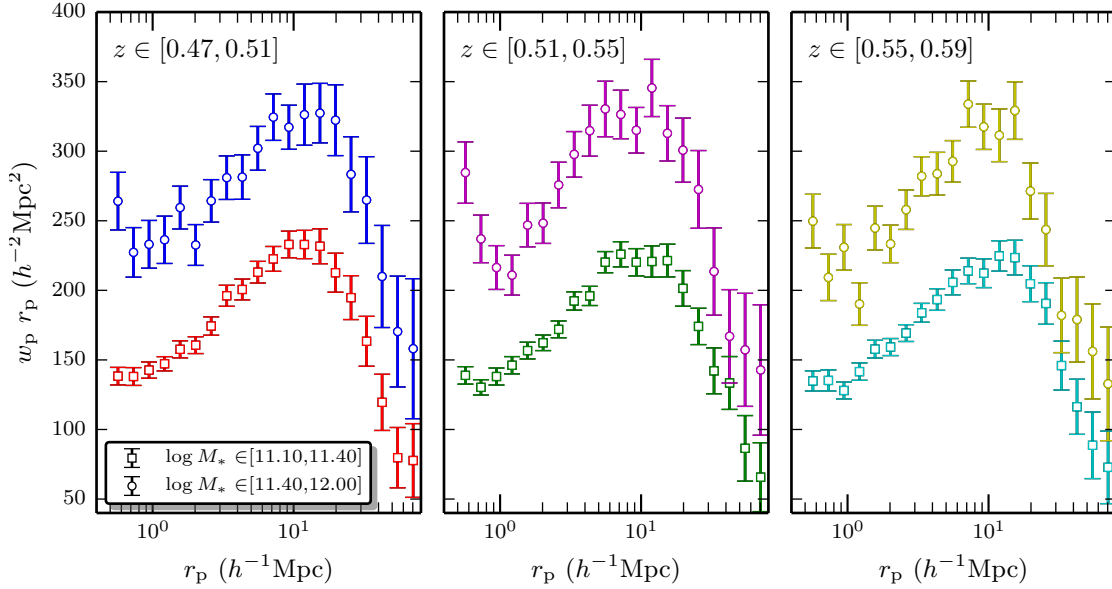


Figure 2. The stellar mass dependence of the projected clustering signal at fixed redshift is displayed in each of the panels for three different redshift bins. Data points with errorbars show the clustering measurements of the different subsamples shown in Figure 1. Squares with errorbars correspond to the stellar mass bin $\log M_*/h_{70}^{-2}M_\odot \in [11.10, 11.40]$ while circles with errorbars correspond to the stellar mass bin $\log M_*/h_{70}^{-2}M_\odot \in [11.40, 12.00]$. The line-of-sight integration length used to project the redshift space correlation function is $60 h^{-1}\text{Mpc}$. At fixed redshift, the clustering amplitude increases strongly with the stellar mass of galaxies.

from our choice of comoving coordinates. Another component of shear, γ_\times , which is a 45° rotated component from the tangential shear, should be statistically consistent with zero for weak gravitational lensing (but potentially nonzero for shape distortions due to systematic errors). Hence we can use the measured γ_\times as a monitor of a possible residual systematics in the lensing measurement.

For each pair of lens and source galaxies, we compute the tangential ellipticity component using

$$e_t = -e_1 \cos 2\phi - e_2 \sin 2\phi, \quad (8)$$

where ϕ is defined as the angle measured from right ascension direction to a line connecting the lens and source galaxies at source galaxy position. Using spherical trigonometry, the angle ϕ is given in terms of the galaxy positions (α, δ) as

$$\begin{aligned} \cos \phi &= \frac{\cos \delta_1 \sin(\alpha_2 - \alpha_1)}{|\sin \theta|} \\ \sin \phi &= \frac{-\sin \delta_1 \cos \delta_2 + \cos \delta_1 \cos(\alpha_2 - \alpha_1) \sin \delta_2}{|\sin \theta|}, \end{aligned} \quad (9)$$

where the angles with subscripts “1” or “2” denote the coordinate components for the lens or source galaxies, respectively, and θ is the separation angle between the galaxies on the sphere:

$$\cos \theta = \sin \delta_1 \sin \delta_2 + \cos \delta_1 \cos \delta_2 \cos(\alpha_1 - \alpha_2). \quad (10)$$

The 45° rotated component, e_\times , is also similarly computed.

While the lens equation (Eq. 6) is for a single source redshift z_s , we take into account the uncertainty in the posterior distribution of the source galaxy photometric redshift. This uncertainty dominates the small uncertainty in the spectroscopic redshift estimate of lens CMASS galaxies.

We follow the method of Mandelbaum et al. (2013), and estimate the average projected mass density profile, $\Delta\Sigma(R)$ in

Eq. (6), as

$$\Delta\Sigma(R) = \frac{\sum_{\text{ls}} w_{\text{ls}} e_t^{(\text{ls})} \left[\langle \Sigma_{\text{cr}}^{-1} \rangle^{(\text{ls})} \right]^{-1}}{(1 + K(R)) \sum_{\text{ls}} w_{\text{ls}}}, \quad (11)$$

where the summation runs over all the pairs of source-lens galaxies separated by the projected radius R to within a given bin width, the superscripts “l” or “s” stand for lens or source galaxies, respectively, and $\langle \Sigma_{\text{cr}}^{-1} \rangle^{(\text{ls})}$ is the critical density averaged with the photo- z PDF for each source-lens pair, defined as

$$\langle \Sigma_{\text{cr}}^{-1} \rangle^{(\text{ls})} \equiv \frac{\int_0^\infty dz_s \Sigma_{\text{cr}}^{-1}(z_1, z_s) P(z_s) dz_s}{\int_0^\infty dz_s P_s(z_s)}. \quad (12)$$

Here the integration is performed from $z = 0.025$ to $z = 3.475$ with the interval of $\Delta z = 0.05$, following the full $P(z)$ information from the CFHTLenS catalog. We set $\Sigma_{\text{cr}}^{-1}(z_1, z_s) = 0$ at $z_s < z_1$ in the above calculation. The above equation automatically corrects for a possible dilution of the lensing signal caused by non-vanishing probability that a source galaxy is at $z_s < z_1$. The weight w_{ls} is defined as

$$w_{\text{ls}} = w_1 w_s \left(\langle \Sigma_{\text{cr}}^{-1} \rangle^{(\text{ls})} \right)^2, \quad (13)$$

where w_1 is defined by Eq. (2), w_s is the weight given by the CFHTLenS catalog described in Section 3.1, and the factor $\left(\langle \Sigma_{\text{cr}}^{-1} \rangle^{(\text{ls})} \right)^2$ downweights pairs that are close in redshift and therefore are inefficient in weak lensing and vice versa. The overall factor $(1 + K(R))$ is introduced in Eq. (11) as recommended in Miller et al. (2013). This factor corrects for a multiplicative shear bias, and is implemented after the stacking average, rather than on a per-galaxy basis. The calibration

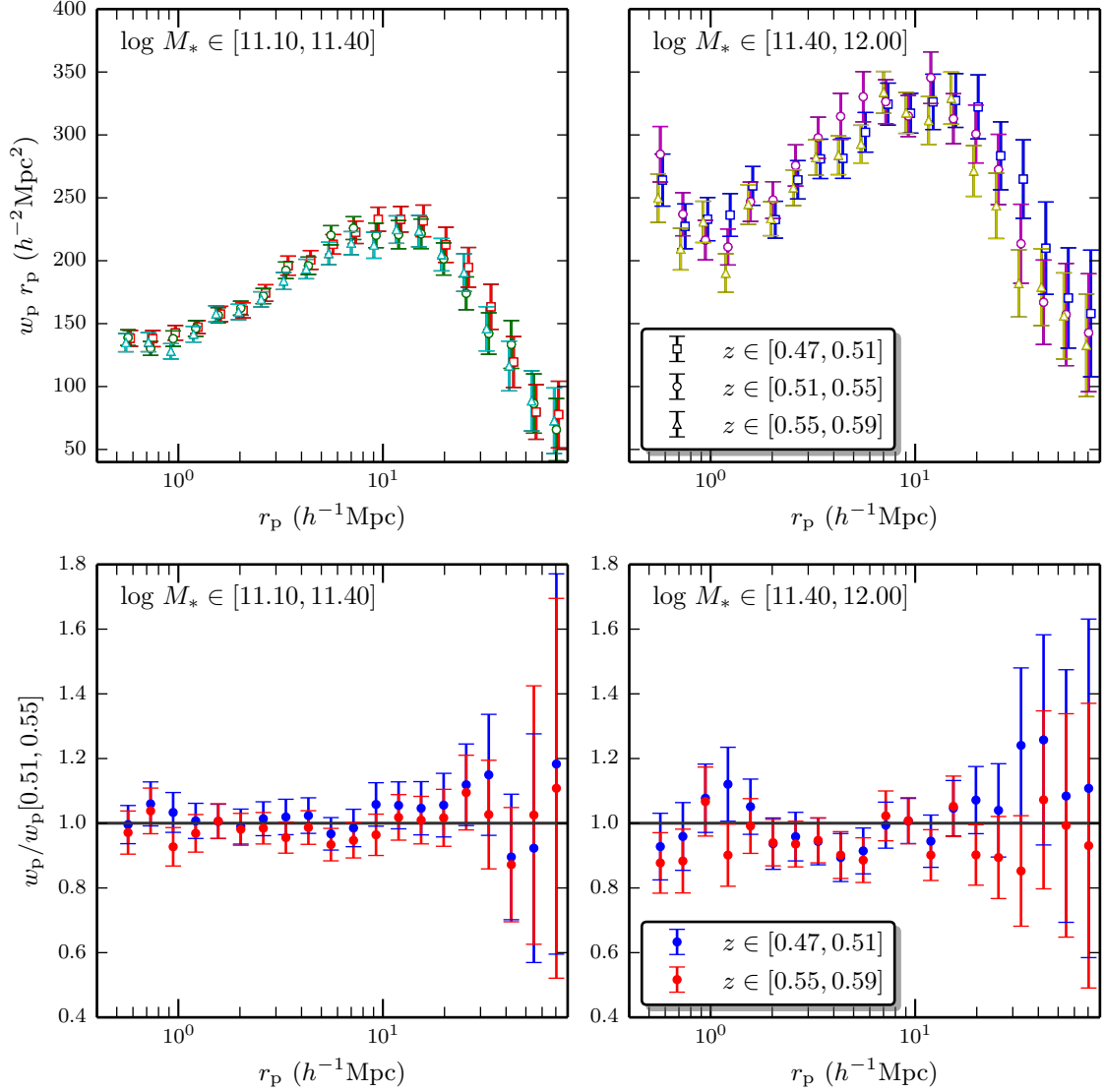


Figure 3. The upper left and right panels display the redshift dependence of the clustering signal at fixed stellar mass for two different stellar mass bins. Data points with errorbars show the clustering measurements of the different subsamples shown in Figure 1. In each panel, squares with errorbars, circles with errorbars, and triangles with errorbars are used to denote the measurement of clustering in the redshift bins $[0.47, 0.51]$, $[0.51, 0.55]$ and $[0.55, 0.59]$, respectively. The line-of-sight integration length used to project the redshift space correlation function is $60 h^{-1} \text{Mpc}$. We have shifted the lowest (highest) redshift bin points to the right (left) by a small amount for clarity. For fixed stellar mass bins, the clustering amplitude varies very weakly with redshift. The bottom panels show the ratio of the measured clustering of galaxies at redshifts $[0.47, 0.51]$ and $[0.55, 0.59]$ to that at redshift $[0.51, 0.55]$ using filled blue and open red circles, respectively. At fixed stellar mass, the clustering does not vary significantly with redshift.

factor is calculated as

$$1 + K(R) = \frac{\sum_{\text{ls}} w_{\text{ls}} (1 + m^{(\text{ls})})}{\sum_{\text{ls}} w_{\text{ls}}}, \quad (14)$$

where $m^{(\text{ls})}$ is the multiplicative bias factor defined in Miller et al. (2013).

For a radial binning for the lensing profile, we set the innermost bin to $R_{\text{min}} = 0.0245 h^{-1} \text{Mpc}$ and employ logarithmically-spacing binning given by $\Delta R/R = 0.4$ (about 6 bins in one decade of radial bin spacing).

3.3. Correcting Lensing Systematic Errors with Random Catalogs

The shear profile measured according to the method given in the preceding section might still be contaminated by resid-

ual systematic effects inherent in the data. One possible systematic error is a dilution of the lensing signal caused when including “source” galaxies, which are actually physically associated with the lens galaxy (or its halo), into the stacking analysis. Another one is a possible residual systematic in the shape measurement, e.g., caused by an imperfect correction of optical distortion across the field of a camera. In this section, following the method in Mandelbaum et al. (2005), we use random catalogs provided by the SDSS-III/BOSS collaboration (Anderson et al. 2014), which is appropriately down-sampled to match our subsamples as described in Section 2.2, to test and correct for these systematic effects. We use random catalogs which consist of 100 times more points than the number of CMASS galaxies, and divide them into 100 realizations to estimate the systematic uncertainties in the following measurements.

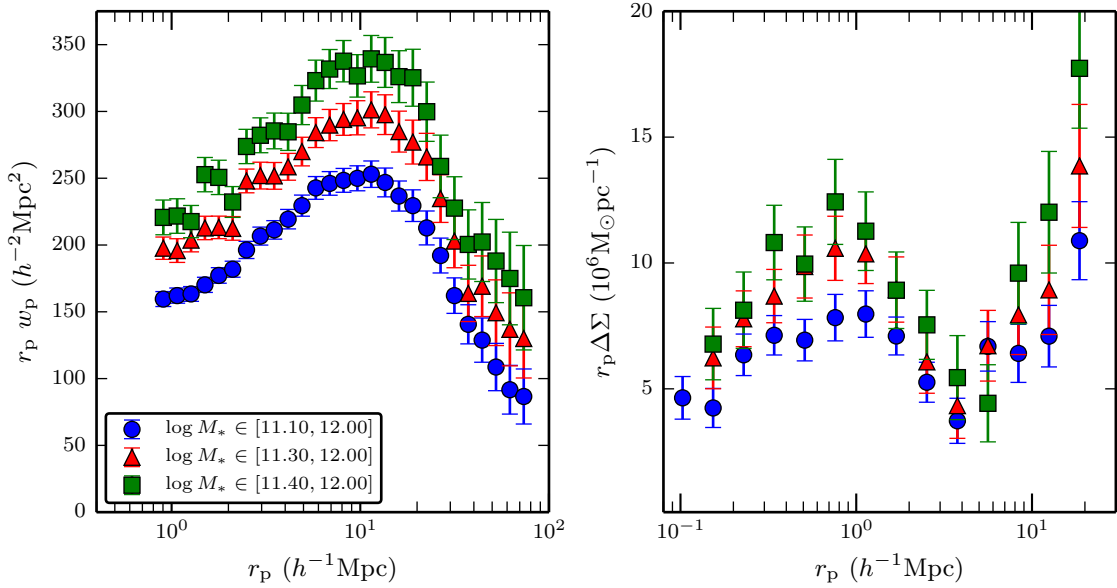


Figure 4. The clustering (left) and the lensing (right) signal measurements for subsamples in the redshift range $z \in [0.47, 0.59]$ but with stellar mass threshold cuts $\log M_* > 11.10, 11.30$ and 11.40 are shown using blue circles with errors, red triangles with errors and green squares with errors, respectively. The line of sight integration length used to project the redshift-space correlation function is $100 h^{-1} \text{Mpc}$ for all the three subsamples. These measurements will be used to constrain the halo occupation distribution parameters of galaxies as well as the cosmological parameters in Paper II.

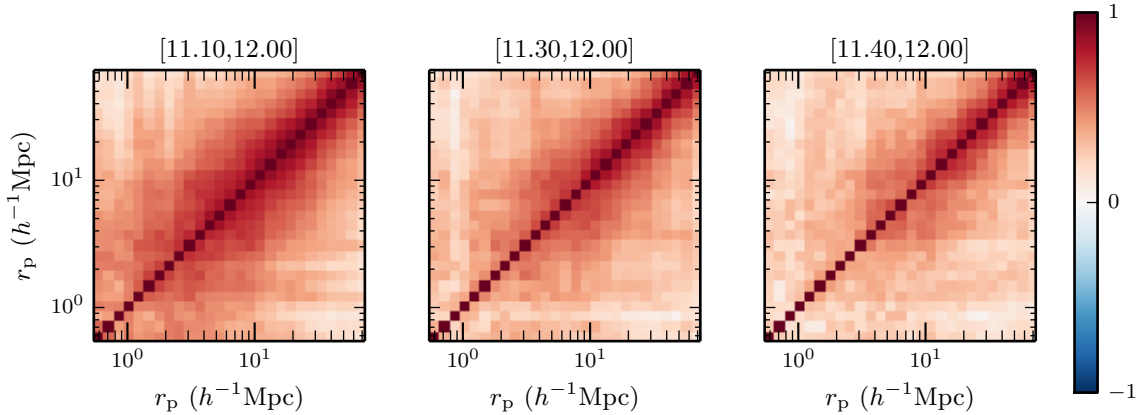


Figure 5. The correlation matrix of the clustering measurements for the subsamples, estimated by using 192 jack-knife samples. The covariance will be used while calculating the likelihood of the clustering measurements given the parameters.

3.3.1. Boost Factor

If some of the galaxies in the source sample are physically associated with a lens galaxy, they will dilute the lensing signal (because they are not lensed). For instance, this is the case if source galaxies are in the same halo of a lens galaxy. This contamination can be estimated by searching for an excess in the number counts of source galaxies in the region of lens galaxies compared to the random distribution. To study the possible excess, we can use the random catalogs that are randomly distributed on the sky, but are generated mimicking the redshift distribution of CMASS lens galaxies. Thus, taking into account the weights, we estimate the *boost* factor defined as

$$B(R) = \frac{\sum_{l_s} w_l w_s \left(\langle \Sigma_{\text{cr}}^{-1} \rangle^{(l_s)} \right)^2 / \sum_l w_l}{\sum_{r_s} w_r w_s \left(\langle \Sigma_{\text{cr}}^{-1} \rangle^{(r_s)} \right)^2 / \sum_r w_r}, \quad (15)$$

where the superscript “ r ” stands for random catalogs, and w_r is the weight for random-lens, at each projected radius R . For an ideal source catalog, $B(R) = 1$, while $B(R) > 1$ if there is a contamination by physically-associated source galaxies.

The left panel of Figure 7 shows the boost factor we measured for our subsample A, where the errorbars are estimated from the scatters of random realizations. The small scales at $R \lesssim 100 h^{-1} \text{kpc}$ display $B(R) < 1$, implying that the number of source galaxies behind the CMASS lens galaxies is smaller than the random distribution, which is not expected from physically-associated source galaxies. A possible origin of $B(R) < 1$ is that a contamination from light of foreground CMASS galaxies reduces the efficiency of detecting source galaxies. The CMASS galaxies are indeed the brightest galaxies in the redshift range in the SDSS catalog, and can be too bright (perhaps causing saturated images) for a much deeper survey such as CFHTLenS. Given that these details rely on the detection of objects in the CFHTLenS *lensfit* processing, we are not in a position to investigate this issue further. An-

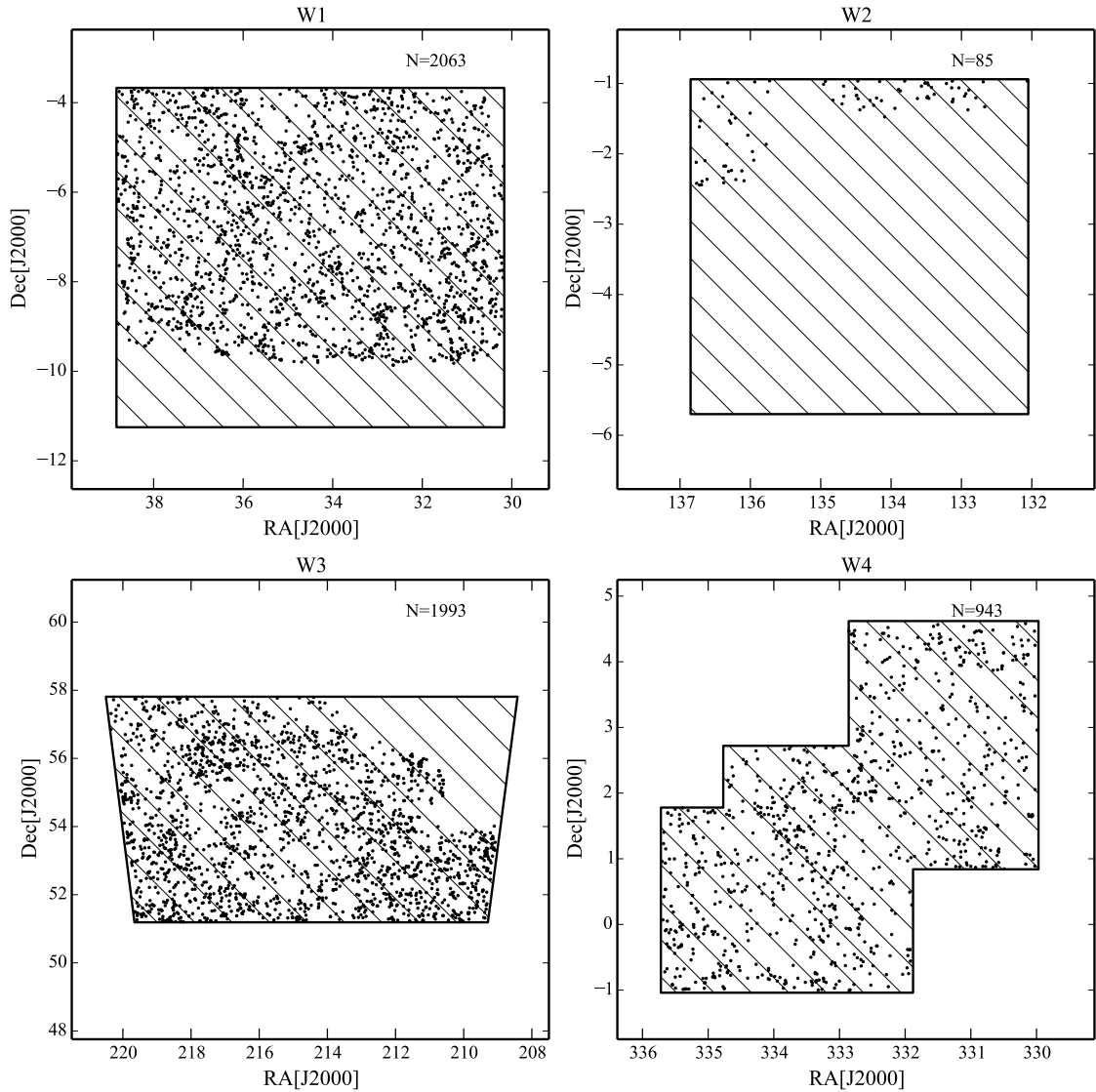


Figure 6. Distribution of our fiducial CMASS galaxy subsample (subsample A) in each of the four CFHTLenS fields as labeled at the top of each panel. The number of CMASS galaxies in each CFHTLenS field is given in the upper right of each panel. The hatched regions denote CFHTLenS fields. The CMASS galaxy subsample in this paper is selected based on their redshift and stellar mass estimates so that the subsample constitutes approximately volume-limited sample and physically-similar population of galaxies (see Section 2.1 and Figure 1 for details).

other possibility is sky-subtraction. The size of sky mesh is 128 pixels¹⁴, which corresponds to $\sim 100 h^{-1}$ kpc at the redshift of CMASS galaxies. Therefore an over-subtraction of the sky might be a possible origin of $B(R) < 1$ at the small radii. Magnification can also affect the observed counts of galaxies near bright objects. Duncan et al. (2014) showed a deficit is expected for the similar magnitude depth¹⁵. Because of the difficulty in identifying the origin of possible systematic errors on small scales, in the following analysis we do not use data at scales smaller than $100 h^{-1}$ kpc (we use different cuts for other subsamples, which are described later). On the other hand, as shown on the plot, the boost factor is consistent with unity at scales larger than $100 h^{-1}$ kpc, meaning that a contamination of physically-associated galaxies with CMASS

galaxies is negligible. Thus we need not adopt the boost factor correction for the CMASS lensing at $R > 100 h^{-1}$ kpc. For comparison, we also plot in Figure 7 the boost factor measured for brighter CFHT galaxies with $\text{mag}_i < 21.5$. In this case, $B(R) > 1$ at $R \lesssim 1 h^{-1}$ Mpc, comparable with a virial radius of massive halos. This result implies that some of the bright galaxies are physically associated with CMASS galaxies, even if their photo- z 's are higher than the CMASS galaxy redshift.

3.3.2. Testing Lens Signal of Random Catalogs

We can also use the random catalogs of CMASS galaxies for testing possible residual systematic errors in the shape measurement of CFHTLenS source galaxies. Since the random points are randomly distributed on the sky, we should not detect any coherent tangential distortion of CFHTLenS galaxy shapes around the random points, if the shape measurement is not contaminated by systematic errors. This test

¹⁴ priv. comm. with T. Erben.

¹⁵ On the other hand, they showed an excess as expected for a bright sample $\text{mag}_i < 21.5$.

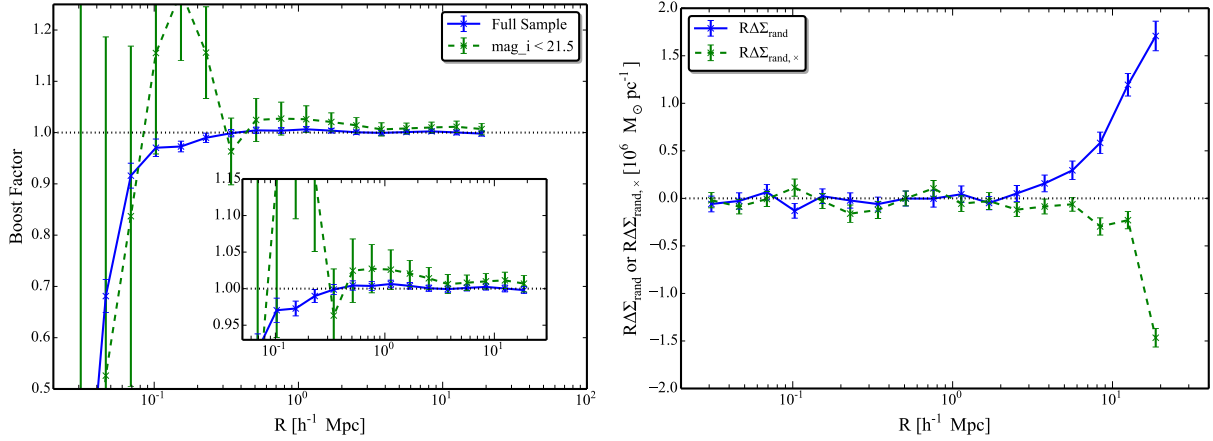


Figure 7. *Left panel:* A “boost factor” $B(R)$, which measures an excess or deficiency in the number of the CMASS-lens and CFHT-source galaxy pairs compared to random point and CFHT-source pairs, where the random catalogs are generated mimicking the redshift distribution of our subsample A. The errorbars are estimated from the standard deviations of the results for 100 random catalogs. The x -axis is the projected comoving radius between the source and lens (or random point) pairs. The expanded plot is shown in the inset at lower right. The solid curve denotes the boost factor for our fiducial subsample of CFHTLenS galaxies, showing that the boost factor is consistent with unity except at small radii $R \lesssim 100 h^{-1}\text{kpc}$ (see text for discussion). For comparison, the dashed curve is the boost factor for the brighter sample with $\text{mag}_i < 21.5$; $B(R) > 1$ at radii $R \lesssim 1 h^{-1}\text{Mpc}$, indicating that some of the CFHTLenS galaxies are physically associated with CMASS galaxies, such as galaxies in the same host halos. *Right panel:* The lensing signals for the CMASS random catalogs for our subsample A, which are measured by stacking the tangential (the blue curve) or 45° rotated (the green curve) components of the CFHTLenS galaxy ellipticities around the random points. Since the random points are randomly distributed on the sky, the signals should vanish within the errorbars if the shape measurement is not contaminated by residual systematic errors. The results show some deviation from zero at the large radii, $R \gtrsim 10 h^{-1}\text{Mpc}$, indicating residual systematic errors (see text for discussion).

can be done by using the random points instead of CMASS galaxy positions in Eq. (11).

The right panel of Figure 7 shows the tangential and 45° rotated distortion profile measured from the random catalogs for our subsample A. While the distortion is consistent with zero within the errorbars at $R \lesssim 3 h^{-1}\text{Mpc}$, the larger radii show an increasing deviation from zero. Thus the larger radius scales indicate residual systematic errors in the shape measurement. The projected radius $R = 10 h^{-1}\text{Mpc}$ for the CMASS mean redshift $z \approx 0.53$ corresponds to about 1° , comparable with the field-of-view of CFHT/MegaCam. Thus the systematic errors are likely due to an imperfect PSF correction in the galaxy shape measurement, or more precisely an imperfect correction of the optical distortion of the camera, which tends to cause a tangential or radial pattern of the PSF ellipticities in the edge of the field of view (Hamana et al. 2013). Since the source and random-point pairs of larger radii are preferentially sensitive to a coherent PSF anisotropy in the edge of field-of-view, the result indicates such a residual systematic error. In the following analysis, we correct for the lensing signals of CMASS galaxies by subtracting the random signal in Figure 7 from the measured signal. As described in Mandelbaum et al. (2005) (see also Mandelbaum et al. 2013), this correction rests on the assumption that the distribution of lens galaxies is uncorrelated with residual systematics in the shape measurements. This assumption holds in our analysis because the lens catalog and the shape measurements are taken from completely different datasets, the SDSS and CFHTLenS data. The size of correction is consistent with zero at small radii, and increases to 10-15% of the measured signals at large radii at $R \sim 10 h^{-1}\text{Mpc}$.

3.4. CMASS Galaxy-galaxy Lensing Signal

In Figure 8, we present the CMASS galaxy-galaxy lensing signals for our subsample A, after correcting for the systematic errors as we described above. As can be found from the

lower panel, the signal in the 45° rotated component is consistent with zero over all the radii we consider. The upper panel shows the tangential distortion, which shows the expected trends of decreasing signal as the projected radius increases. The cumulative signal-to-noise ratio is about 26. For comparison, we show the lensing signal of the SDSS LRG catalog using the CFHTLenS source catalog and the same lensing measurement procedures (for details of the LRG lensing measurement, see Appendix A). The CMASS galaxy lensing signal is about 40% smaller than the LRG lensing signal, suggesting that the CMASS galaxies preferentially reside in less massive halos. As a verification of our lensing measurement, we also show the LRG signal measured from the independent data, the SDSS source catalog, in RM13. The CFHTLenS and SDSS LRG lensing signals are in excellent agreement with each other. To be more quantitative, the inverse-variance weighted ratio of the two LRG signals from these different surveys with completely independent shape measurements and photo- z , averaged over all the radial bins, is 1.006 ± 0.046 . We note that the LRG lensing measurement is performed under the cosmological model of $\Omega_m = 0.25$ and $\Omega_\Lambda = 0.75$ to make it consistent with the measurement in RM13.

We comment on a possible systematic bias in the CMASS lensing signal that may be caused by a residual bias in the photo- z estimates of source galaxies, to the level of $\delta z \sim 0.02$, due to photo- z outliers as claimed in Erben et al. (2013). We checked that even shifting the photo- z PDF, $P(z)$, for all the source galaxies by $\delta z = \pm 0.02$ in the analysis causes only a few percent shift in the lensing signal. Hence we ignore the possible photo- z bias in the following results.

Another systematic uncertainty might come from the difference between the CMASS galaxy subsample in the entire BOSS region and that in the CFHTLenS region. We compare the probability distribution of the stellar mass, $P(\log M_*)$, and that of the redshifts, $P(z)$, for our subsamples in these regions in the panels of Figure 9. Although the stellar mass distri-

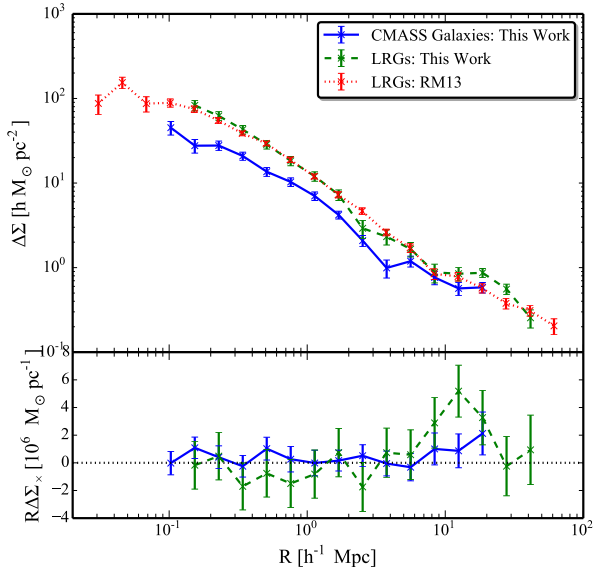


Figure 8. The solid curves show the average surface mass density profile measured from the CMASS and CFHTLenS galaxy-galaxy weak lensing, where the errorbars are estimated from 100 random catalogs of CMASS galaxies. In this measurement we corrected for the possible contamination of residual systematic errors in Figure 7; we subtracted the lensing signals of the random catalogs from the measured CMASS lensing signals at each radial bin. For comparison, the dashed curve shows the lensing profile for the SDSS luminous red galaxies (LRGs), measured from the CFHTLenS catalog using the same measurement procedures. The dotted curve is the LRG lensing measured from the SDSS catalog, which shows an excellent agreement with the CFHTLenS measurement within the errorbars. The lower panel presents the measurements of non-lensing mode for the CMASS and LRG catalogs.

butions in the CFHT region is not particularly special, the redshift distributions shows some noticeable differences, presumably due to the structures in the CFHT field. We assessed the systematics of the differences in the redshift distribution by including a weight $w_{\text{sys}}(z) = P^{\text{CMASS}}(z)/P^{\text{CFHT}}(z)$, where $P^{\text{CMASS}}(z)$ and $P^{\text{CFHT}}(z)$ is the spectroscopic distribution in the entire CMASS region and that in the CFHTLS region, respectively, when calculating the weak lensing signal. The differences in the lensing signal when including this weight are of the order 2 percent, much smaller than our errorbars on the lensing signal. We therefore conclude that this weight is not needed for the analysis, and that the subsample of CMASS galaxies in the CFHT fields is sufficiently close to a fair sample for our purposes.

To construct a model interpretation of the CMASS lensing signal, we need to compute the error covariance matrix of the lensing profile. There are two sources of the statistical errors. First, since the number of source galaxies used is finite, the intrinsic shape noise contributes to the errors. In fact this is a dominant source of the errors over the range of radial scales we consider. The shape noise is naively expected to scale as $\sigma_e/\sqrt{N_{\text{pair}}}$, where σ_e is the rms intrinsic ellipticity combined with the rms ellipticity measurement error, per component, and N_{pair} is the number of source-lens pairs used in the lensing measurement of a given radius. However, the scaling does not hold for large radii, because the same source galaxies are used multiple times as the stacking annuli of such large radii overlap for different lens CMASS galaxies. The other noise source arises from a projection effect: large-scale structure along the same line-of-sight to the CMASS lens galaxy, at different redshifts, causes statistical scatters in the distortion of CFHTLenS galaxies. We estimate these contributions

by computing the covariance matrix of lensing signals from the 100 random catalog realizations. The random catalog enables us to estimate both the covariance contributions of the shape noise and the projection effect. We note that we cannot use the jackknife method for the covariance estimation of the lensing measurements. Unlike for the BOSS clustering measurements, the area of the CFHTLS region which overlaps with BOSS is too small to have a sufficiently large enough resampling of the CFHTLenS regions for the jackknife method (especially for the large separation radii). The left panel of Figure 10 shows the correlation coefficients of the covariance matrix for subsample A. The large separation radii display a strong correlation between neighboring bins. Figure 11 shows the ratio of the diagonal covariance elements to the naively-expected shape noise error, where the shape noise expectation is computed taking into account the weights. At larger scales, the ratio is significantly greater than unity, meaning that the projection effect and the correlated shape noise become significant at these radii.

The lensing signals for the three subsamples A, B and C of CMASS galaxies are shown in the right panel of Figure 4. We perform the same analysis for subsamples B and C, such as the systematic tests by boost factor and correction for imperfect PSF modeling by random signals. For subsamples B and C we find that the boost factor is significantly smaller than one at scales below $150 h^{-1} \text{kpc}$, and thus discard the lensing signal at these scales. As the stellar mass threshold increases, the amplitude of lensing signal becomes larger. Correlation coefficients of subsamples B and C are shown in the middle and right panel of Figure 10, respectively.

We also explore the redshift dependence of the lensing signal. In Figure 12, we show lensing signals for three redshift subsamples with the lowest stellar mass threshold. The lensing signals do not vary substantially with redshift, similar to the behaviour of the clustering signal.

4. DISCUSSION AND CONCLUSIONS

In this paper, we have shown the clustering and lensing measurements of the SDSS-III/CMASS galaxies at $z \approx 0.53$. In our analysis, we constructed a subsample of galaxies so that it constitutes an approximately stellar mass limited sample ($\log M_*/h_{70}^{-2}$ in $[11.10, 12.0]$) over the redshift range $z \in [0.47, 0.59]$, with approximately constant number density (subsample A). This subsample of galaxies was used to measure the projected clustering signal with a total signal-to-noise ratio of 56 for scales $0.85 h^{-1} \text{Mpc} \lesssim r_p \lesssim 80 h^{-1} \text{Mpc}$ (see Figure 4). We then made use of the publicly available galaxy shape and photometric redshift catalogs compiled by the CFHTLenS collaboration based on deeper, higher quality imaging data from the CFHTLS. This imaging catalog has an overlap of a mere 105 deg^2 with the BOSS footprint, but it allows measurement of the weak gravitational lensing signal of the BOSS galaxies, selected in the same way to our fiducial subsample, with a signal-to-noise ratio of 26 for $0.1 h^{-1} \text{Mpc} \lesssim r_p \lesssim 20 h^{-1} \text{Mpc}$. Thus we showed significant detections for both the clustering and weak lensing signals for the BOSS CMASS galaxies at the highest redshift for such a joint analysis, $z \sim 0.5$.

To test for possible systematics arising from our sample selection we also studied the clustering and lensing signals for two other subsamples within the same redshift range, but with higher thresholds in stellar mass, $\log M_*/h_{70}^{-2} M_{\odot} \in [11.30, 12.0]$ and $\log M_*/h_{70}^{-2} M_{\odot} \in [11.40, 12.0]$ (subsamples

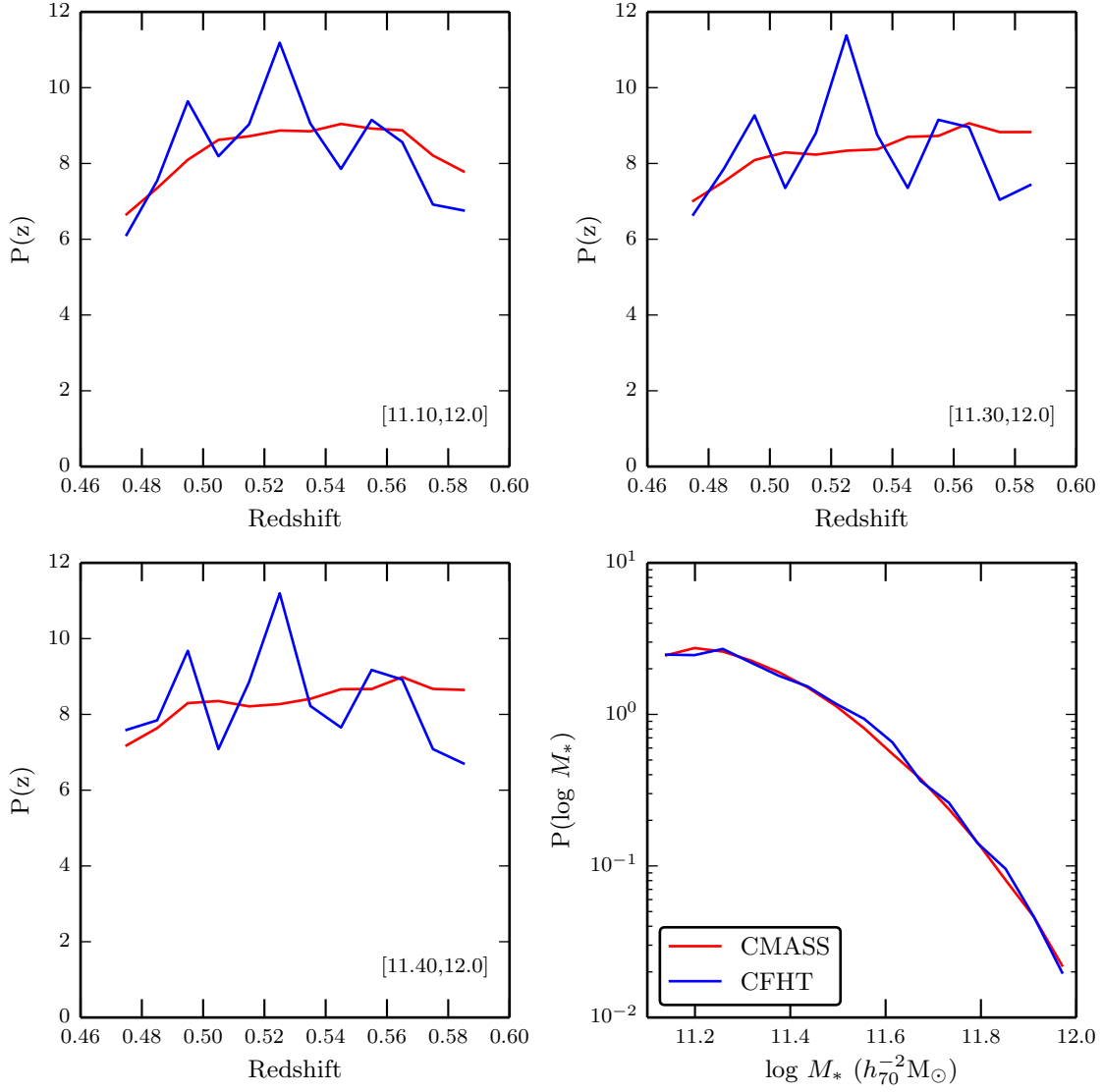


Figure 9. The comparison of the redshift distributions of galaxies in the CFHTLS fields (blue solid line) and those in the CMASS fields (red solid line) for the three stellar mass subsamples we use for our analysis are shown in the top left, top right and bottom left panels. The bottom right panel shows a similar comparison but for the stellar mass distribution of galaxies. The stellar mass distribution of the CFHT subsample appears fairly representative of that of the entire CMASS population. The redshift distribution shows noisy deviations due to structures in the CFHT regions.

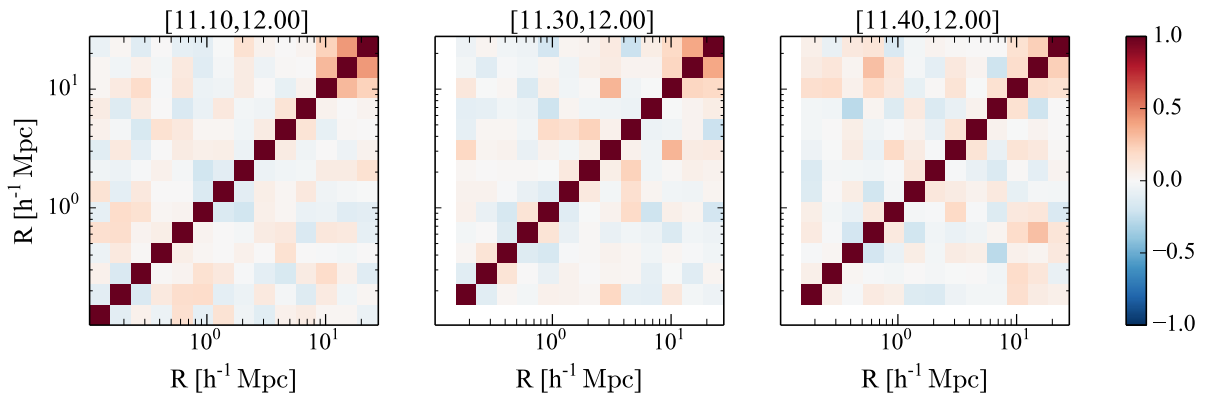


Figure 10. Correlation coefficients of the error covariance matrix for the CMASS galaxy weak lensing signal for our subsamples, where the covariance matrix is computed from the 100 random catalogs.

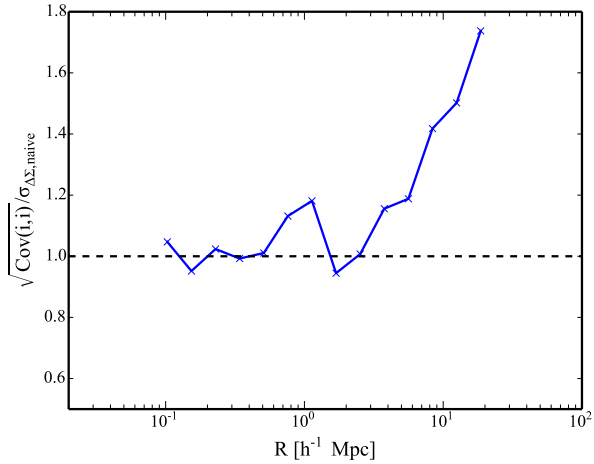


Figure 11. The square root of the diagonal covariance elements relative to the naively-expected shape noise, where the latter is estimated by scaling the shape noise by $\sqrt{N_{\text{pair}}}$ (the total number of source-lens galaxy pairs at each radial bin). To estimate the shape noise expectation, we properly take into account the weights. At $R \lesssim$ a few h^{-1} Mpc, the shape noise is a dominant source of the errors, while the projection effect and the correlated shape noise become significant at larger radii.

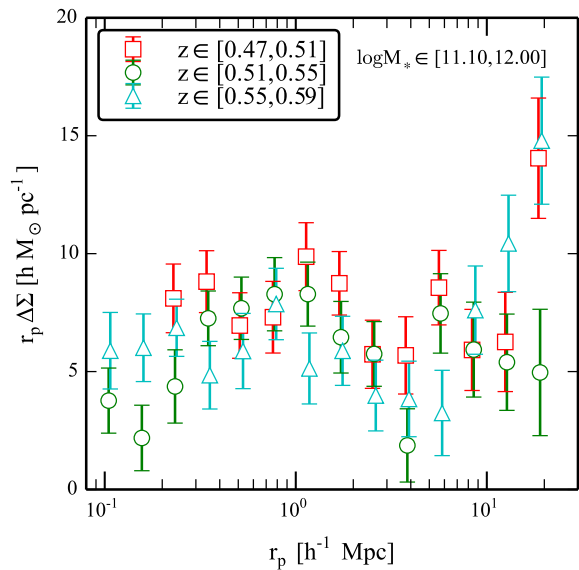


Figure 12. The lensing signals of redshift subsamples at fixed stellar mass threshold $\log M_* \in [11.10, 12.00]$. There is no substantial variation with redshift.

B and C respectively). The subsamples of higher stellar mass thresholds progressively display the higher amplitudes in the clustering and weak lensing signals (Figures 2 and 4). These results suggest that the CMASS galaxies of higher stellar masses tend to reside in more massive halos. On the other hand, we found the weak redshift dependence of the signals for each subsample (Figures 3 and 12). This result allows us to employ an effectively signal redshift bin over the redshift range when making the model interpretation.

In Paper II, we will use the clustering and lensing measurements of the CMASS galaxies to explore the dark matter-galaxy connection in the framework of the halo model. By fitting the halo occupation parameters and cosmological parameters to both of these observables simultaneously, we will

explore the physical nature of CAMSS galaxies and their host dark matter halos as well as constrain cosmological parameters.

ACKNOWLEDGMENTS

We greatly thank Hong Guo, Anatoly Klypin, Francisco Prada, Ramin Skibba, and Simon White for useful comments during the SDSS internal review. HM and RM greatly thank Alexie Leauthaud, Melanie Simet, Lance Miller, Catherine Heymans, Ludovic Van Waerbeke, and Hendrik Hildebrandt for useful discussion about the CFHTLenS catalog.

HM is supported by Japan Society for the Promotion of Science (JSPS) Postdoctoral Fellowships for Research Abroad and JSPS Research Fellowships for Young Scientists. MT is supported in part by JSPS KAKENHI (Grant Number: 23340061), by World Premier International Research Center Initiative (WPI Initiative), MEXT, Japan, and by the FIRST program ‘Subaru Measurements of Images and Redshifts (SuMIRe)’, CSTP, Japan. RM is supported in part by the Department of Energy Early Career Award program. This work was supported in part by the National Science Foundation under Grant No. PHYS-1066293 and the hospitality of the Aspen Center for Physics.

Funding for SDSS-III has been provided by the Alfred P. Sloan Foundation, the Participating Institutions, the National Science Foundation, and the U.S. Department of Energy Office of Science. The SDSS-III web site is <http://www.sdss3.org/>.

SDSS-III is managed by the Astrophysical Research Consortium for the Participating Institutions of the SDSS-III Collaboration including the University of Arizona, the Brazilian Participation Group, Brookhaven National Laboratory, University of Cambridge, Carnegie Mellon University, University of Florida, the French Participation Group, the German Participation Group, Harvard University, the Instituto de Astrofísica de Canarias, the Michigan State/Notre Dame/JINA Participation Group, Johns Hopkins University, Lawrence Berkeley National Laboratory, Max Planck Institute for Astrophysics, Max Planck Institute for Extraterrestrial Physics, New Mexico State University, New York University, Ohio State University, Pennsylvania State University, University of Portsmouth, Princeton University, the Spanish Participation Group, University of Tokyo, University of Utah, Vanderbilt University, University of Virginia, University of Washington, and Yale University.

This work is based on observations obtained with MegaPrime/MegaCam, a joint project of CFHT and CEA/IRFU, at the Canada-France-Hawaii Telescope (CFHT) which is operated by the National Research Council (NRC) of Canada, the Institut National des Sciences de l’Univers of the Centre National de la Recherche Scientifique (CNRS) of France, and the University of Hawaii. This research used the facilities of the Canadian Astronomy Data Centre operated by the National Research Council of Canada with the support of the Canadian Space Agency. CFHTLenS data processing was made possible thanks to significant computing support from the NSERC Research Tools and Instruments grant program.

REFERENCES

- Abazajian, K. N., et al. 2009, *ApJS*, 182, 543
- Ahn, C. P., et al. 2012, *ApJS*, 203, 21
- Aihara, H., et al. 2011, *ApJS*, 193, 29
- Anderson, L., et al. 2012, *MNRAS*, 427, 3435
- , 2014, *MNRAS*, 441, 24

- Aubourg, É., et al. 2014, ArXiv e-prints
- Baldauf, T., Smith, R. E., Seljak, U., & Mandelbaum, R. 2010, *Phys. Rev. D*, 81, 063531
- Benítez, N. 2000, *ApJ*, 536, 571
- Beutler, F., et al. 2011, *MNRAS*, 416, 3017
- Blake, C., et al. 2011, *MNRAS*, 418, 1707
- Blanton, M. R., Lin, H., Lupton, R. H., Maley, F. M., Young, N., Zehavi, I., & Loveday, J. 2003, *AJ*, 125, 2276
- Bolton, A. S., et al. 2012, *AJ*, 144, 144
- Cacciato, M., van den Bosch, F. C., More, S., Li, R., Mo, H. J., & Yang, X. 2009, *MNRAS*, 394, 929
- Cacciato, M., van den Bosch, F. C., More, S., Mo, H., & Yang, X. 2013a, *MNRAS*, 430, 767
- Cacciato, M., van Uitert, E., & Hoekstra, H. 2013b, ArXiv e-prints
- Coe, D., Benítez, N., Sánchez, S. F., Jee, M., Bouwens, R., & Ford, H. 2006, *AJ*, 132, 926
- Cole, S., et al. 2005, *MNRAS*, 362, 505
- Dawson, K. S., et al. 2013, *AJ*, 145, 10
- Doi, M., et al. 2010, *AJ*, 139, 1628
- Duncan, C. A. J., Joachimi, B., Heavens, A. F., Heymans, C., & Hildebrandt, H. 2014, *MNRAS*, 437, 2471
- Eisenstein, D. J., et al. 2001, *AJ*, 122, 2267
- , 2011, *AJ*, 142, 72
- Erben, T., et al. 2013, *MNRAS*, 433, 2545
- Feldman, H. A., Kaiser, N., & Peacock, J. A. 1994, *ApJ*, 426, 23
- Fischer, P., et al. 2000, *AJ*, 120, 1198
- Fukugita, M., Ichikawa, T., Gunn, J. E., Doi, M., Shimasaku, K., & Schneider, D. P. 1996, *AJ*, 111, 1748
- Gillis, B. R., et al. 2013, *MNRAS*, 431, 1439
- Gunn, J. E., et al. 1998, *AJ*, 116, 3040
- , 2006, *AJ*, 131, 2332
- Guo, H., Zehavi, I., & Zheng, Z. 2012, *ApJ*, 756, 127
- Hamana, T., Miyazaki, S., Okura, Y., Okamura, T., & Futamase, T. 2013, ArXiv e-prints
- Heymans, C., et al. 2012, *MNRAS*, 427, 146
- Hildebrandt, H., et al. 2012, *MNRAS*, 421, 2355
- Hinshaw, G., et al. 2013, *ApJS*, 208, 19
- Kazin, E. A., et al. 2010, *ApJ*, 710, 1444
- Komatsu, E., et al. 2011, *ApJS*, 192, 18
- Kroupa, P. 2001, *MNRAS*, 322, 231
- Landy, S. D., & Szalay, A. S. 1993, *ApJ*, 412, 64
- Leauthaud, A., et al. 2012, *ApJ*, 744, 159
- Li, R., Mo, H. J., Fan, Z., Cacciato, M., van den Bosch, F. C., Yang, X., & More, S. 2009, *MNRAS*, 394, 1016
- LSST Science Collaboration et al. 2009, ArXiv e-prints
- Lupton, R., Gunn, J. E., Ivezić, Z., Knapp, G. R., & Kent, S. 2001, in *Astronomical Society of the Pacific Conference Series*, Vol. 238, *Astronomical Data Analysis Software and Systems X*, ed. F. R. Harnden, Jr., F. A. Primini, & H. E. Payne, 269
- Mandelbaum, R., Seljak, U., Kauffmann, G., Hirata, C. M., & Brinkmann, J. 2006, *MNRAS*, 368, 715
- Mandelbaum, R., Slosar, A., Baldauf, T., Seljak, U., Hirata, C. M., Nakajima, R., Reyes, R., & Smith, R. E. 2013, *MNRAS*, 432, 1544
- Mandelbaum, R., et al. 2005, *MNRAS*, 361, 1287
- Marston, C., et al. 2013, *MNRAS*
- Miller, L., Kitching, T. D., Heymans, C., Heavens, A. F., & van Waerbeke, L. 2007, *MNRAS*, 382, 315
- Miller, L., et al. 2013, *MNRAS*, 429, 2858
- Miyazaki, S., et al. 2012, in *Society of Photo-Optical Instrumentation Engineers (SPIE) Conference Series*, Vol. 8446, *Society of Photo-Optical Instrumentation Engineers (SPIE) Conference Series*
- Mo, H. J., & White, S. D. M. 1996, *MNRAS*, 282, 347
- More, S., Miyatake, H., Mandelbaum, R., Takada, M., Spergel, D., Brownstein, J., & Schneider, D. P. 2014, ArXiv e-prints
- More, S., van den Bosch, F. C., Cacciato, M., More, A., Mo, H., & Yang, X. 2013, *MNRAS*, 430, 747
- Padmanabhan, N., et al. 2008, *ApJ*, 674, 1217
- Percival, W. J., et al. 2010, *MNRAS*, 401, 2148
- Pier, J. R., Munn, J. A., Hindsley, R. B., Hennessy, G. S., Kent, S. M., Lupton, R. H., & Ivezić, Ž. 2003, *AJ*, 125, 1559
- Planck Collaboration et al. 2013, ArXiv e-prints
- Reid, B. A., Seo, H.-J., Leauthaud, A., Tinker, J. L., & White, M. 2014, *MNRAS*, 444, 476
- Reid, B. A., et al. 2012, *MNRAS*, 426, 2719
- Rest, A., et al. 2013, ArXiv e-prints
- Ross, A. J., et al. 2012, *MNRAS*, 424, 564
- Saito, S., Takada, M., & Taruya, A. 2011, *Phys. Rev. D*, 83, 043529
- Samushia, L., et al. 2014, *MNRAS*, 439, 3504
- Schlegel, D., White, M., & Eisenstein, D. 2009, in *ArXiv Astrophysics e-prints*, Vol. 2010, *astro2010: The Astronomy and Astrophysics Decadal Survey*, 314
- Schlegel, D. J., Finkbeiner, D. P., & Davis, M. 1998, *ApJ*, 500, 525
- Seljak, U., et al. 2005, *Phys. Rev. D*, 71, 043511
- Sheth, R. K., & Tormen, G. 1999, *MNRAS*, 308, 119
- Simpson, F., et al. 2013, *MNRAS*, 429, 2249
- Smee, S. A., et al. 2013, *AJ*, 146, 32
- Smith, J. A., et al. 2002, *AJ*, 123, 2121
- Spergel, D., et al. 2013, ArXiv e-prints
- Strauss, M. A., et al. 2002, *AJ*, 124, 1810
- Sullivan, M., et al. 2011, *ApJ*, 737, 102
- Suzuki, N., et al. 2012, *ApJ*, 746, 85
- Takada, M., et al. 2014, *PASJ*, 66, 1
- Tegmark, M., et al. 2004, *Phys. Rev. D*, 69, 103501
- Tinker, J. L., et al. 2012, *ApJ*, 745, 16
- van Uitert, E., Hoekstra, H., Velander, M., Gilbank, D. G., Gladders, M. D., & Yee, H. K. C. 2011, *A&A*, 534, A14
- Velander, M., et al. 2013, ArXiv e-prints
- Yoo, J., Tinker, J. L., Weinberg, D. H., Zheng, Z., Katz, N., & Davé, R. 2006, *ApJ*, 652, 26
- York, D. G., et al. 2000, *AJ*, 120, 1579
- Zehavi, I., et al. 2011, *ApJ*, 736, 59

APPENDIX

CALCULATION OF LRG LENSING SIGNAL

In this section we describe details of our measurement of the SDSS LRG lensing signal shown in Figure 8. We select LRGs (Eisenstein et al. 2001) in the regions overlapping with CFHTLenS fields from the SDSS DR7 catalog (Abazajian et al. 2009). Out of 62,081 LRGs of the entire SDSS fields, 534 LRGs are selected. The number of LRGs in each CFHTLenS field is 149 in W1, 0 in W2, 338 in W3, and 47 in W4, respectively. We use the same weighting scheme as that in RM13, which is given as

$$w_1 = \frac{w_{\text{rad}} w_{\text{fc}}}{C}, \quad (\text{A1})$$

where w_{rad} is the weight to account for the radial selection function, w_{fc} is the fiber collision weight, and C is the “sector completeness” that accounts for the redshift success rate. These weights are available from the publicly-available LRG catalog (see Appendix A in Kazin et al. 2010 for the details).

We perform systematic tests of the LRG lensing signal using random catalogs as described in Section 3.3. We generate 100 realizations of the random catalogs for the overlapping regions of the SDSS and CFHTLenS fields. The left panel of Figure 13 shows the boost factor for the LRG sample. As we found from the boost factor for our subsample of the CMASS galaxies in Figure 7, the small scales displays $B(R) < 1$. Thus we do not use the lensing measurements at $R < 150 h^{-1} \text{kpc}$ (up to the 4th bin). While the boost factor is consistent with unity at the larger radii, it is slightly smaller than unity by a few per cent at the intermediate radii. Since our lensing signal remains consistent with RM13 (Figure 8) within this offset, we do not adopt the boost factor correction for the LRG lensing signals. The right panel shows the lensing measurements for the random catalogs of LRGs. As seen for the measurements of the CMASS random catalogs in Figure 7, the large radii show non-zero signals, indicating residual systematics in the shape measurements (see Section 3.3.2 for the discussion). We correct for the LRG lensing signal by subtracting the random signal from the measured signal. Figure 8 shows the measurement of LRG lensing signal, compared to the measurement in RM13 that was done using the independent data, the SDSS imaging galaxies, for the galaxy shape measurements. The CFHTLenS and SDSS measurements for LRG lensing show an excellent agreement with each other.

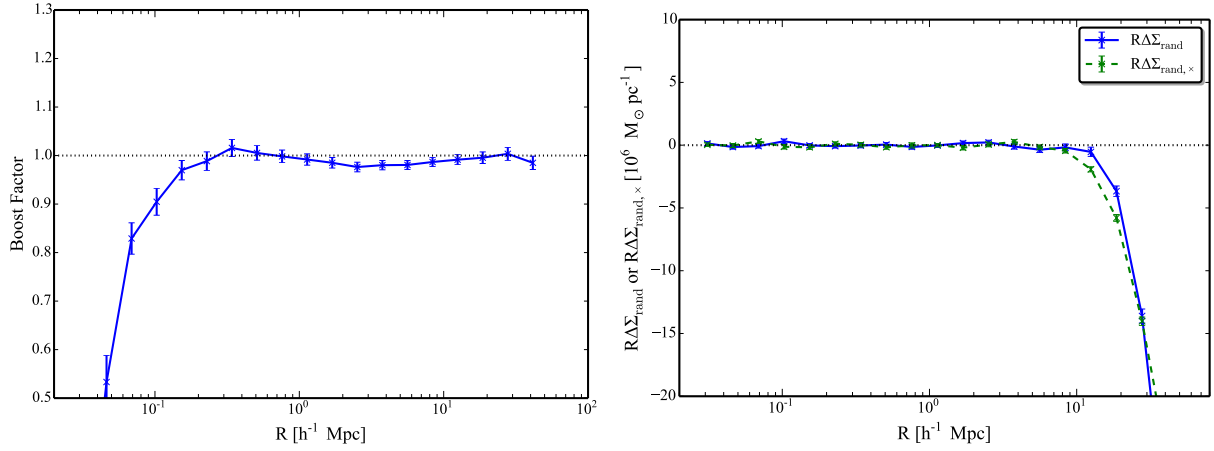


Figure 13. *Left panel:* A boost factor of LRGs. Although the boost factor is slightly smaller than unity at intermediate scales, this does not affect the consistency between our CFHTLenS LRG signal and the SDSS LRG lensing signal described in Section 3.4 (see text for discussion). *Right:* The random signal of LRGs. As seen in the CMASS galaxy measurement, the random signal is not consistent with zero, which implies a coherent PSF anisotropy at the edge of the field-of-view is not fully corrected. We corrected for this effect by subtracting the random signal from a measured lensing signal.